

This article appeared in a journal published by Elsevier. The attached copy is furnished to the author for internal non-commercial research and education use, including for instruction at the authors institution and sharing with colleagues.

Other uses, including reproduction and distribution, or selling or licensing copies, or posting to personal, institutional or third party websites are prohibited.

In most cases authors are permitted to post their version of the article (e.g. in Word or Tex form) to their personal website or institutional repository. Authors requiring further information regarding Elsevier's archiving and manuscript policies are encouraged to visit:

<http://www.elsevier.com/copyright>



Contents lists available at ScienceDirect

Nuclear Instruments and Methods in Physics Research A

journal homepage: www.elsevier.com/locate/nima

Topical Review

Laser-produced MeV electrons and hard X-ray spectroscopic diagnostics

J.F. Seely^{a,*}, L.T. Hudson^b^a Naval Research Laboratory, Space Science Division, Washington, DC 20375, USA^b National Institute of Standards and Technology, Gaithersburg, MD 20899, USA

ARTICLE INFO

Available online 6 December 2009

Keywords:

X-ray source size
MeV electron propagation
K-shell transitions
X-ray spectroscopy

ABSTRACT

A new spectroscopic technique for the measurement of the sizes of hard X-ray sources produced by the irradiation of solid-density targets by intense laser radiation is discussed. The technique is based on the source broadening of K shell spectral lines from targets irradiated by intense picosecond laser pulses. The spectra are recorded by a modified Cauchois type spectrometer, where the detector is placed far behind the Rowland circle where source broadening dominates instrumental resolution. The laser irradiation with focused intensity greater than 10^{18} W/cm² produces relativistic electrons that propagate from the focal spot into the surrounding target material with mm range. The energetic electrons produce 1 s electron ionization and K shell radiation with picosecond duration that can be utilized for transient radiography of dense objects including evolving dense plasmas. However, the hard X-ray source has mm lateral size when extended targets are utilized while a much smaller source size (of order 10 μ m) is necessary for high-resolution point projection radiography. The lateral source size can be greatly reduced by using targets with limited aspect to the radiography object such as thin foils and wires, but the brightness of these sources is greatly reduced compared to thick planar targets. Studies indicate that the electron range and source size can also be reduced by utilizing an electrically resistive target material such as teflon. In this case the electron propagation from the focal spot is inhibited by a weak return current and incomplete space-charge neutralization. These experimental results are important not only for producing a small hard X-ray source for picosecond radiography but also for reducing the lateral propagation of energetic electrons that can be detrimental to fast-ignition fusion.

Published by Elsevier B.V.

1. Introduction

Transmission crystal (Laue diffraction) X-ray spectrometers have been developed to record hard X-ray spectra generated by irradiating metal targets with intense laser pulses. These spectrometers are based on the Cauchois geometry, which implements a cylindrically curved crystal and a Rowland circle with diameter equal to the radius of curvature of the crystal [1,2]. During in-house testing of the spectrometer performance using laboratory Mo and W sources, it was noticed that the spectral resolving power increased when the detector was placed beyond the conventionally-employed Rowland circle [3]. This increased resolving power, achieved without loss of signal, enabled the observation of the $K\alpha_1$, $K\alpha_2$, $K\beta_1$, and $K\beta_2$ transitions while using spectrometers with relatively small dimensions, typically less than 0.5 m, and with relatively high throughput.

Shown in Fig. 1 is a schematic of a typical transmission crystal module utilized in these spectrometers. X-rays are incident on the

convex side of a cylindrically bent crystal, are diffracted through a slit, and are recorded by a planar detector placed on or behind the Rowland circle. Metal filters located at the slit provide K absorption edges in the continuum spectra for *in situ* calibration of the X-ray energy scale. A pinhole with separate filtration is on the center axis of the spectrometer and produces an image of the source. The relative positions of the pinhole image and the dispersed spectral image indicate the instrument pointing. Massive lead shielding is present on the front of the module and at the slit, and there is no line-of-sight path (except through the pinhole) between the source and detector. This geometry facilitates shielding of the detector from the energetic X-ray flux from the source, and in the case of plasmas produced by intense laser irradiation, shielding from energetic protons and electrons.

Several transmission crystal spectrometers have been developed and utilized for the study of laser-produced plasmas with varying pulse lengths and energies on target. The high-energy X-ray spectrometer (HXS) implemented a cylindrically bent quartz (10-11) crystal covering the 12–70 keV energy range with modest ($E/\Delta E \approx 100$) resolving power [4,5]. The high-energy electronic X-ray (HENEX) spectrometer implemented a curved quartz (10-11) crystal covering the 11–40 keV range with

* Corresponding author. Tel. +1 202 767 3529.

E-mail address: john.seely@nrl.navy.mil (J.F. Seely).

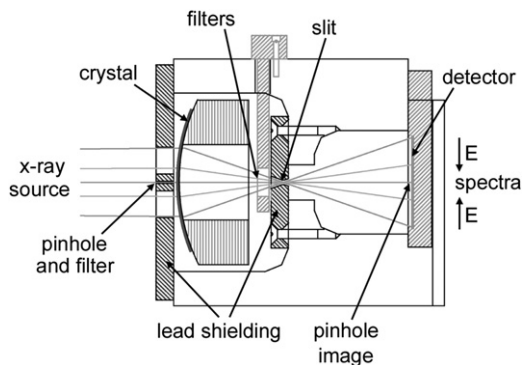


Fig. 1. Schematic of the HXS transmission crystal spectrometer module.

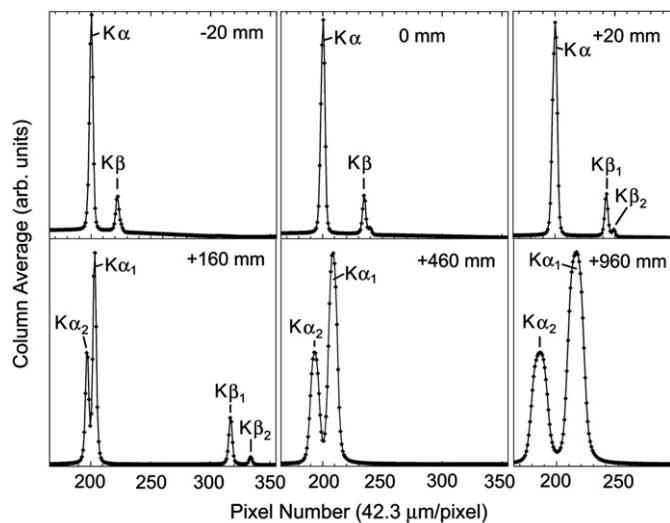


Fig. 2. The Mo spectra recorded by the HXS spectrometer by placing the detector near the focal circle and at distances up to 960 mm behind the focal circle. The spectrum recorded on the focal circle is indicated by 0 mm. For each distance behind the focal circle, the spectrum is plotted as a column average in the direction along the spectral lines (perpendicular to the dispersion direction) and as a function of pixel number in the dispersion direction, where the pixel width is 42.3 μm .

resolving power greater than 300 along with four reflection crystals covering lower energy ranges [6–8]. The dual crystal spectrometer (DCS) implemented two quartz (10–11) crystals, bent to 119 and 254 mm radii of curvature, and covering the 10–50 keV and the 20–120 keV energy ranges [9]. These instruments were based on spectrometers developed at the National Institute of Standards and Technology (NIST) for the measurement of the peak kilovoltage of medical X-ray sources [10–12].

The spectra of Fig. 2 illustrate the increase in spectral resolution observed when the detector was placed at increasing distances beyond the Rowland circle of the HXS spectrometer. In this case, the X-rays were produced by a Mo microfocus source, and image plates were placed up to 960 mm beyond the focal circle (the spectrum recorded on the focal circle is indicated by 0 mm in Fig. 2).

A geometrical model was developed to understand and model the experimental spectra recorded at various distances behind the Rowland circle [13]. It was found that the source broadening in units of distance on the detector that is produced by an extended source with lateral width w , in the plane of dispersion and perpendicular to the spectrometer axis, is $wD/(S+R)$ where D is the distance of the detector behind the Rowland circle, R is the

crystal radius of curvature (the Rowland circle diameter), and S is the source-to-crystal distance. Thus on the Rowland circle $D=0$ and the source broadening is zero, and behind the Rowland circle, $D > 0$ and the magnification factor is $D/(S+R)$, the ratio of the detector distance and the source distance with respect to the Rowland circle. Thus the lateral source width w can be measured from the source broadening of the spectral lines recorded behind the Rowland circle.

This is the basis for the new spectroscopic technique for measuring the lateral source size that determines the spatial resolution achieved in hard X-ray radiography. The technique has the benefit of utilizing the (mono-energetic) spectral lines emitted from the X-ray source, and the source size can be characterized as a function of X-ray energy by using a range of spectral line energies. In addition, in the case of intense laser irradiation, the lateral X-ray source size results from the propagation of energetic electrons from the laser focal spot of typical size 10 μm into the surrounding target material where 1 s ionization and K shell emission occurs. Thus the source size is a measure of the electron range and can be used to characterize the energetic electron distribution, which is important for understanding the laser–target interaction mechanism and for the fast-ignition fusion concept.

In order to accurately measure the source broadening of the spectral lines, it is necessary to remove the detector resolution contribution to the observed line shapes. Thus it was necessary to determine the modulation transfer function (MTF) and the point spread function (PSF) of the Fuji type SR and MS image plates used in the experiments. This was done using three techniques [14]: (1) the MTF was measured using a test object with linear openings and bars with line pair (LP) frequencies in the range 0.25–10 LP/mm, and the PSF was derived from the MTF, (2) the PSF was determined from the edge transfer function produced by sharp edge that was opaque to the X-rays, and (3) the PSF was determined directly from the shapes of narrow spectral lines recorded on the Rowland circle. The results were consistent and indicated that the point spread functions of the SR and MS image plates were Gaussian in shape with full-width at half-maximum (FWHM) value of 0.13 mm and Lorentzian with 0.19 mm FWHM, respectively for the X-ray energies studied. The image plate scanner added a small additional broadening.

The spectra from laboratory sources with known source sizes were recorded by several different spectrometers, and the spectral line widths were in good agreement with the geometrical model. For example, shown in Fig. 3 is a comparison of the dispersion, spectral line widths, and resolving power recorded by the DCS spectrometer using a quartz (10–11) crystal bent to 254 mm radius and positioned 1200 mm from the W anode with a 1.8 mm source size. Three SR image plates were positioned at distances of 140, 700, and 1260 mm behind the Rowland circle, and the image plates were exposed simultaneously. Thus the dispersed W X-ray intensity propagated through the three image plates, and portions of the X-ray fluence were deposited in each image plate and resulted in spectra recorded simultaneously at three distances behind the Rowland circle. The second order K shell spectra were observed at distance of 140 and 700 mm, while at 1260 mm the second order spectra fell beyond the ends of the image plate and were not recorded. In the calculation of the line widths, the SR image plate resolution was set to 0.14 mm and the source size to 1.8 mm. Thus there are no free parameters in the calculation, and there is good agreement between the calculated curves and the experimental data points. As seen in Fig. 3(d), the detector resolution (curve 2) is dominant on the Rowland circle and source broadening (curve 3) is dominant beyond the Rowland circle.

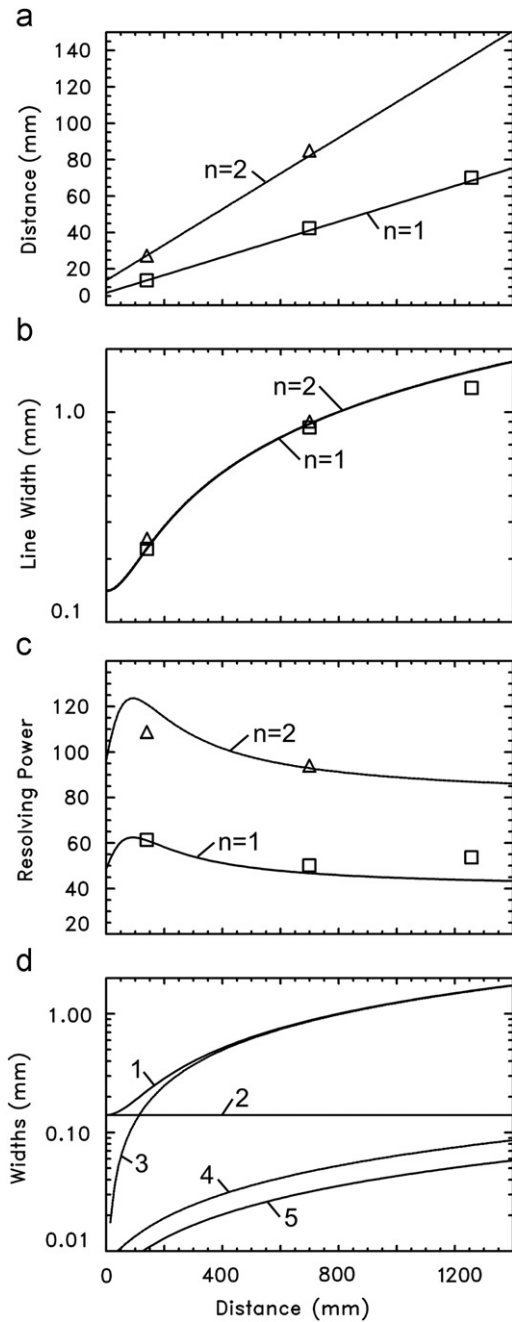


Fig. 3. Comparison of the calculated and measured $W K\beta_1$ results derived from spectra recorded by a quartz (10-11) crystal bent to 254 mm radius as functions of the distance beyond the Rowland circle. Three image plates were positioned at distances of 140, 700, and 1260 mm behind the focal circle, and the image plates were exposed simultaneously. (a) Distance of the $W K\beta_1$ spectral line from the axis of the spectrometer, (b) width of $K\beta_1$ in mm, (c) resolving power of $K\beta_1$, and (d) total and partial line widths from various broadening mechanisms: 1 - total width, 2 - detector resolution, 3 - source size, 4 - crystal thickness, and 5 - natural width of the spectral line.

2. Spectra produced by picosecond laser irradiation

In the initial high-resolution spectra recorded using an intense picosecond laser (the Titan laser at Lawrence Livermore National Laboratory), it was noticed that the spectral lines were broader than expected if the X-rays were emitted from an extent comparable to the laser focus [15]. It was suspected that the broad lines were the result of the propagation of MeV electrons from the focal spot to the surrounding target material and thereby

resulting in a mm size hard X-ray source size that was much larger than the focal spot (of order $10 \mu\text{m}$). The understanding of the source broadening and other spectral line broadening mechanisms, enabled by the geometrical model of the spectrometer [13], guided the design of a spectrometer optimized for the measurement of the source size given the other experimental conditions [16]. That is, the spectrometer parameters (source distance S , crystal radius R , and detector distance D) were selected, within the boundaries imposed by the other experimental constraints, so that source broadening in the spectra recorded behind the Rowland circle dominated over other broadening mechanisms such as crystal thickness, crystal rocking curve, spectrometer aberrations, and natural line width. The optimized spectrometer was developed for the picosecond laser facility at Laboratoire pour L'Utilisation des Lasers Intenses (LULI) at Ecole Polytechnique and was named LULI crystal spectrometer (LCS). This spectrometer utilizes two image plate detectors, one placed on the Rowland circle and another 200 mm behind the focal circle as illustrated in Fig. 4(a). Thus spectra are recorded simultaneously on the Rowland circle, where detector resolution is dominant, and behind the Rowland circle where source broadening is dominant. Using spectra recorded on the same laser shot, the detector resolution can be registered and therefore removed from the source-broadened spectrum allowing accurate determination of the source size.

The overall length of the LCS spectrometer ($S+R+D$) was limited by the desire to fit the entire spectrometer inside the LULI target chamber. The source-to-crystal distance was selected to be $S=600 \text{ mm}$, the Rowland circle diameter (crystal bending radius) was $R=254 \text{ mm}$, and the Rowland circle-to-back detector distance was $D=200 \text{ mm}$ resulting in an overall source to rear-detector length of 1054 mm. When using MS image plates, this optical system has the ability to measure hard X-ray source sizes as small as $200 \mu\text{m}$.

The spectra were recorded by irradiating a variety of targets with a single shot of the LULI PICO2000 laser that typically has 100 J energy, 1 ps pulse duration, $10 \mu\text{m}$ focal spot diameter, and 10^{20} W/cm^2 focused intensity [17]. As shown by Fig. 4(b), the laser beam was incident on the target at a typical angle of $45\text{--}55^\circ$ to the plane of the target surface; the LCS spectrometer viewed the irradiated side of the target at a fixed angle of 90° to the incident laser beam. The target surface could be rotated on

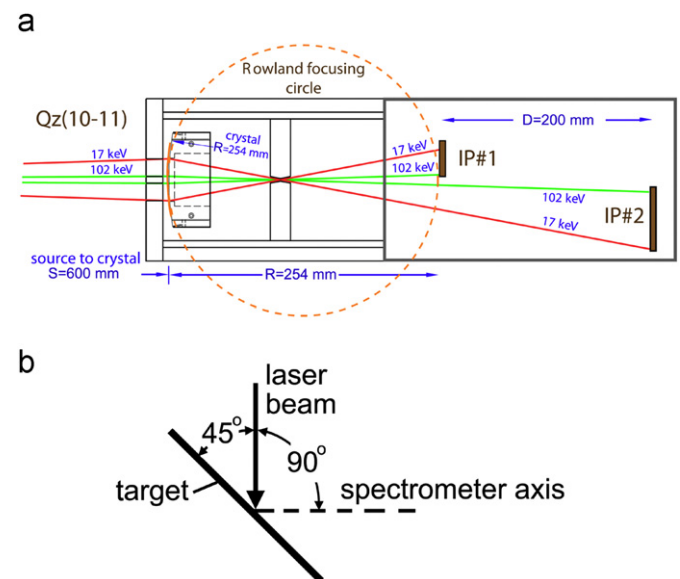


Fig. 4. (a) Schematic of the LCS spectrometer and (b) the target geometry.

different laser shots to vary the laser beam angle of incidence and the spectrometer viewing angle with respect to the target normal.

Typical spectra recorded simultaneously on the same laser shot on a planar CsI target are shown in Fig. 5 and were recorded by (a) an MS image plate on the Rowland circle and (b) an MS image plate positioned 200 mm behind the Rowland circle. The vertical lines in Fig. 5 indicate the energy positions of the characteristic X-ray transitions originating from neutral Cs and I atoms.

Lorentzian functions were fit to the four $K\alpha_1$ and $K\alpha_2$ lines using the least squares technique, and the inferred FWHM values in mm are indicated in Fig. 5. On the Rowland circle, where all mono-energetic rays from an extended source are focused, the FWHM values of the scanned spectral lines are expected to be equal to the FWHM of the point spread function of the MS image plate, 0.19 mm, plus a small additional width contributed by the scanner. While the Cs and I $K\alpha_2$ lines have 0.20 mm widths,

the Cs and I $K\alpha_1$ lines have larger widths of 0.25 and 0.24 mm, respectively. The larger than expected widths of the $K\alpha_1$ features probably result from additional unresolved transitions. The spectral line widths recorded 200 mm behind the Rowland circle, shown in Fig. 5(b), are significantly broader than those recorded on the Rowland circle, and this is attributed to source broadening. The spectrum in Fig. 5(b) has better resolution compared to Fig. 5(a) because the dispersion increases with distance behind the Rowland circle faster than the source broadening.

The Cs and I $K\alpha_1$ lines recorded behind the Rowland circle are broader than the Cs and I $K\alpha_2$ lines in the same spectrum, similar to the trend in the spectrum recorded on the Rowland circle. Understanding the differing widths of the $K\alpha_1$ and $K\alpha_2$ lines in the same spectrum requires a spectrometer with higher resolving power and will be the subject of future experiments.

Fig. 6(a) compares the Cs and I line widths measured behind the Rowland circle from Fig. 5(b) and the line width calculated as a function of source size using the geometrical model of the LCS

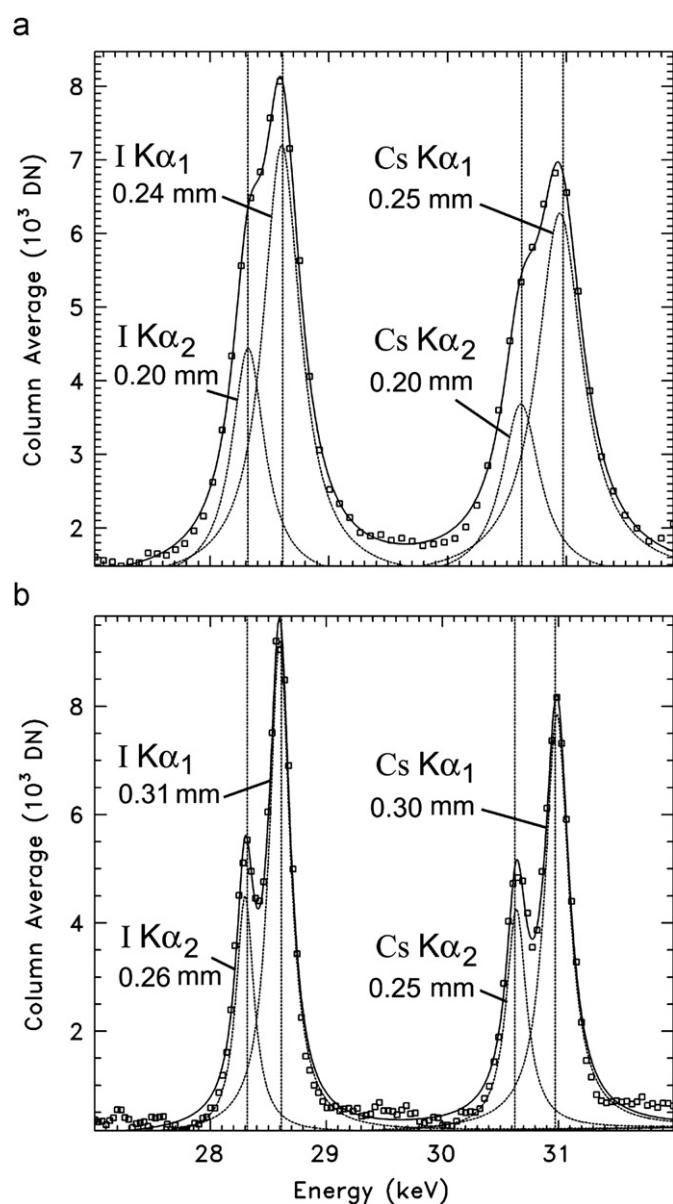


Fig. 5. The spectra from a planar CsI target recorded by placing MS image plates (a) on the Rowland circle and (b) 200 mm behind the Rowland circle. The measured FWHM values (in mm) of the fitted Lorentzian profiles are indicated. The vertical lines indicate the energy positions of the characteristic X-ray transitions originating from neutral Cs and I atoms.

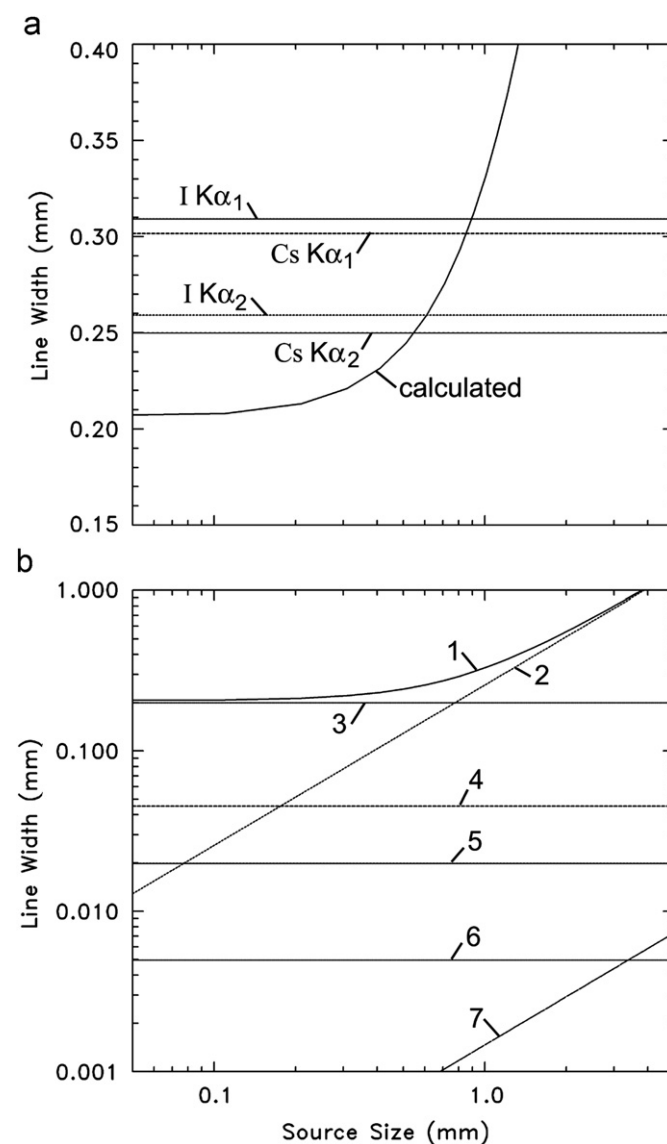


Fig. 6. (a) Comparison of the measured and calculated CsI line widths. (b) The contributions to the calculated line widths as functions of source size where the curve labels are: 1=total line width, 2=source broadening, 3=0.2 mm detector spatial resolution, 4=crystal thickness (0.29 mm) contribution, 5=natural width of the spectral line, 6=crystal rocking curve contribution, and 7=calculated spectrometer aberrations.

spectrometer [13]. The calculated contributions to the line width are shown in Fig. 6(b), where the source broadening becomes significant for source sizes greater than 0.2 mm. Based on the measured line widths, the source size in the lateral direction perpendicular to the spectrometer central axis is inferred to be 0.6 mm. This is much larger than the 10 μm focal spot diameter and results from the lateral propagation of energetic electrons from the focal spot into the surrounding target material.

Energetic electron generation by intense laser irradiation has been previously observed at numerous laser facilities. Early experiments using intense nanosecond neodymium-glass and CO₂ laser irradiation recorded X-ray spectra of low Z elements, typically aluminum, and these studies inferred hot electron energies exceeding 10 keV [18,19]. In addition to electron propagation into buried X-ray fluor layers, lateral energetic electron propagation far outside the focal spot, believed to be guided by strong magnetic and electric fields, was also observed [20,21]. Electron propagation to the backsides of targets and strong return currents along the target support stalks were studied [22–24]. The development of sub-picosecond lasers with focused intensities approaching 10²⁰ W/cm² resulted in the generation of MeV electrons and ions that were believed to be accelerated by the ponderomotive potential into the target and perpendicular to the laser beam [25,26]. The inhibition of fast electron propagation in electrically resistive plastic foams [27] and the recirculation (refluxing) of fast electrons resulting from transient charge separation [28,29] were observed. MeV electron propagation along the surface of targets irradiated by femtosecond laser pulses has also been observed [30–35].

While it is possible that energetic electron propagation along or above the target surface contributes to the hard X-ray emission observed in the present experiments, the analysis of the lateral extent of the emission indicates that the emission primarily results from the propagation of energetic electrons through the target materials.

3. Energetic electron propagation range

The propagation ranges of mono-energetic electrons in various materials were calculated using the NIST ESTAR code [36] and are shown in Fig. 7 as functions of density and for electron energies of

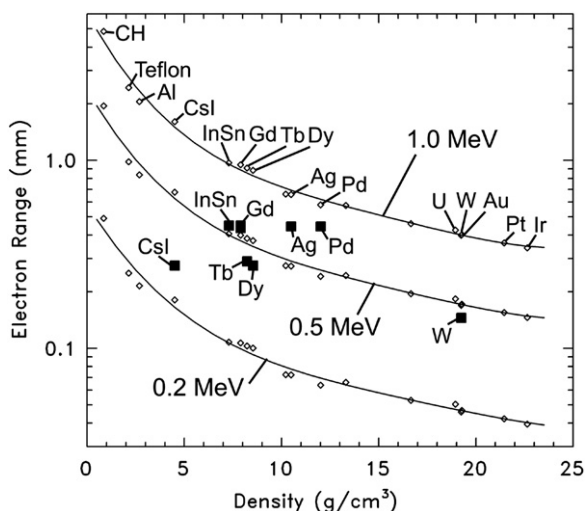


Fig. 7. The calculated electron ranges as functions of material density and for electron energies 0.2, 0.5, and 1.0 MeV. The data points, indicated by the filled square symbols, show the measured extent of the X-ray emission from the laser focal spot.

0.2, 0.5, and 1.0 MeV. Assuming that the energetic electrons propagate radially from the laser focal spot and generate K α emission in the surrounding cold material by 1 s electron ionization, then the half-width of the source, determined from the half-widths of the spectral lines, is a measure of the lateral propagation range from the focal spot. The data points in Fig. 7 (the solid black square symbols) are the determined source half-widths. It is seen in Fig. 7 that the measured source half-widths fall near the 0.5 MeV curve, implying that the typical hot electron energy generated in the focal spot is approximately 0.5 MeV. This first order approximation assumes an 'effective' mono-energetic electron source term and also neglects the effects of electrons propagating into the target and other geometrical and spectrometer line of sight effects. Specifically, since the ESTAR ranges differ from lateral distance in a target by a scattering factor, the inferred energies are a lower bound on the effective electron energy.

We notice that the half-width of the electrically insulating material CsI falls well below the 0.5 MeV curve and the half-widths of the excellent conductors Ag and Pd fall well above the 0.5 MeV curve. This suggests that in these types of experiments energetic electron propagation is inhibited in a good insulator because of the absence of a strong return current that would tend to neutralize the space charge of the expanding energetic electrons. More recent experiments using the LULI 100 TW femtosecond laser, not reported here, confirm that the hard X-ray emission is significantly lower from targets containing Teflon (resistivity > 10¹⁶ Ωm) compared to Al (3 \times 10⁻⁸ Ωm).

Additional experiments were performed using wire targets mounted on plastic washers as illustrated in Fig. 8. The wires were oriented approximately perpendicular to the plane containing the laser beam and the spectrometer axis; see Fig. 4(b). The focal spot was centered on the middle wire, and K-shell spectra were recorded from the irradiated wire material and from the neighboring spectator wires of different materials.

The target shown in Fig. 8(a) consists of a 0.5 mm diameter Dy wire and 0.5 mm Gd wires in contact on each side. The laser was incident at the center of the Dy wire. The observed spectrum is shown in Fig. 9(a) where the vertical lines indicate the energy positions of the characteristic X-ray transitions originating from neutral Dy and Gd atoms. K-shell emission was observed from the irradiated Dy wire and from the two spectator Gd wires. The ratio of the emission from the Gd wires and the Dy wire is 0.42.

The target shown in Fig. 8(b) consists of 0.125 mm diameter wires of W, Ta, Re, and Hf. The observed spectrum is shown in Fig. 9(b) where the vertical lines indicate the energy positions of the characteristic X-ray transitions originating from neutral atoms. K-shell emission was observed from the irradiated central W wire and from the two neighboring Ta wires. The positions of the Re and Hf lines are indicated, but emissions from these outermost wires are absent in the spectrum because energetic electrons do not propagate through the innermost wires to reach the Re and Hf wires.

The ratio of the emission from the Ta wires and the W wire is 1.6. This implies that energetic electrons readily propagated the 0.063 mm distance through the W wire to reach the 0.125 mm diameter Ta wires but did not reach the outlying Re and Hf wires.

The relative K-shell emission from the irradiated and spectator wires can be compared to the energy deposited in the wires during the electron slowing down process since to first order the emission cross-sections and instrumental sensitivities are comparable. Shown in Fig. 10 are the electron energies, calculated using the NIST ESTAR code [36], as functions of the distance from the focal spot in the Dy/Gd and the W/Ta/Re wires and for initial electron energies of 0.4, 0.5, and 0.6 MeV. The

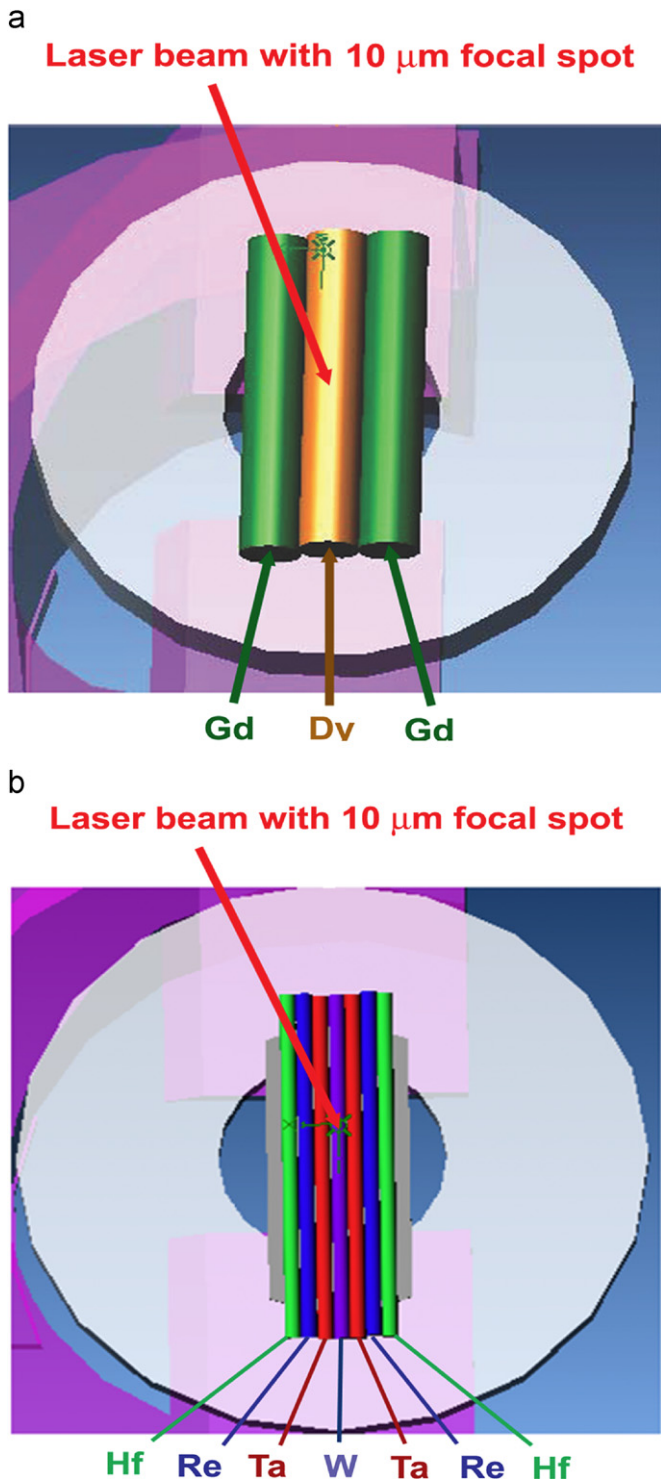


Fig. 8. Schematics of the wire targets. (a) The target composed of an irradiated Dy wire and spectator Gd wires each with 0.5 mm diameter. (b) The target composed of an irradiated W wire and the spectator Ta, Re, and Hf wires each with 0.125 mm diameter.

energies deposited in the wires are listed in Table 1 along with the ratios of the energies deposited in the spectator and the irradiated wires. These ratios can be compared to the observed ratios of the K-shell emission from the spectator and irradiated wires. It is seen that the observed K-shell emission ratio from the Gd and Dy wires, 0.42, is consistent with an initial electron energy of approximately 0.4 MeV. The observed ratio of K-shell emission

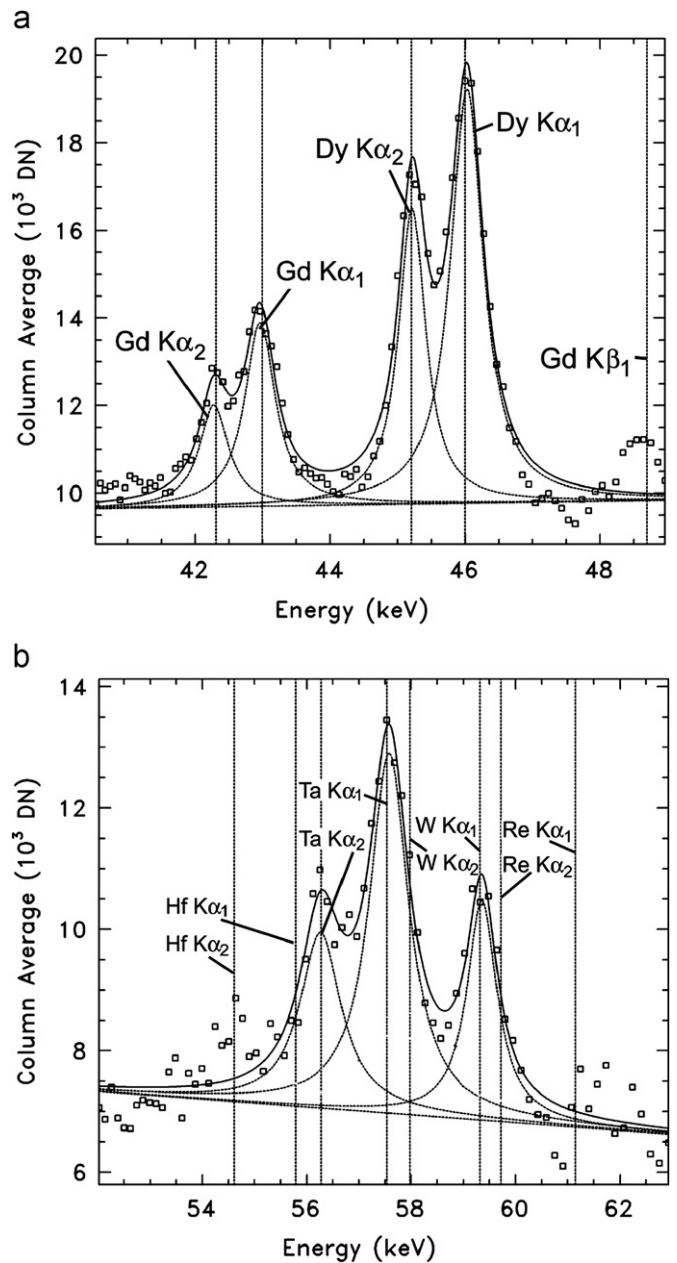


Fig. 9. The spectra from (a) the Dy/Gd wire target and (b) the W/Ta/Re/Hf wire target. The vertical lines indicate the energy positions of the characteristic X-ray transitions originating from neutral atoms. In (a), the spectral features originate in the irradiated Dy wire and the two adjacent Gd wires. In (b), the spectral features originate in the irradiated W wire and the two adjacent Ta wires. The positions of the Re and Hf lines are indicated, but emissions from these outermost wires are absent in the spectrum because energetic electrons do not propagate through the innermost wires to reach the Re and Hf wires.

from the Ta and W wires, 1.6, is consistent with initial electron energy of approximately 0.5 MeV.

The measurement of the extent of the energetic electron propagation from the focal spot into neighboring wires is not significantly affected by electron propagation in other directions such as along the laser beam. Also the spectrometer line of sight does not affect the measurements. The measurements depend only on the known diameters of the wires. Since the electron energies inferred from the propagation ranges in the wire materials, 0.4–0.5 MeV, are in good agreement with the half-widths of the planar target sources shown in Fig. 7, typically

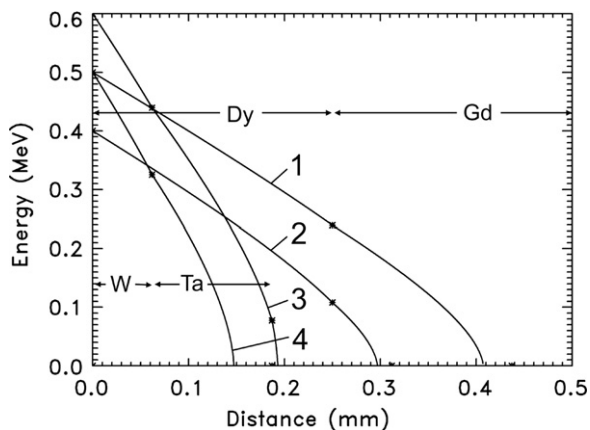


Fig. 10. The calculated energies as functions of propagation distance in the wire materials in the Dy/Gd and W/Ta/Re/Hf targets and for initial electron energies of 0.4, 0.5, or 0.6 MeV. Curve 1: Dy/Gd target and 0.5 MeV initial energy. Curve 2: Dy/Gd target and 0.4 MeV initial energy. Curve 3: W/Ta/Re/Hf target and 0.6 MeV initial energy. Curve 4: W/Ta/Re/Hf target and 0.5 MeV initial energy.

Table 1

The initial electron energies (in MeV), the calculated energies (in eV) deposited in the irradiated wire (Dy or W) and the two spectator wires (Gd or Ta), and the ratios of the deposited energies (Gd/Dy or Ta/W).

Curve number	Energy (MeV)	Dy energy (keV)	Gd energy (keV)	Gd/Dy ratio
1	0.5	261	239	0.92
2	0.4	292	108	0.37
		W energy (keV)	Ta energy (keV)	Ta/W ratio
3	0.6	161	362	2.25
4	0.5	175	325	1.86

The curve number is defined consistently with the curves in Fig. 10.

0.5 MeV, this implies that the planar target source sizes are primarily determined by the electron propagation range in the planar materials.

Thus for both types of targets, planar and wire, the observed lateral extent of the hard X-ray emission is consistent with the slowing down of the energetic electrons in the various target materials with wide-ranging densities. It is unlikely that electrons propagating along the target surface would be so affected by the target density, and plasma electrons outside the target surfaces should show no dependence upon substrate conductivity. These observations indicate that the observed hard X-ray emission primarily results from energetic electrons passing through the target material.

4. Discussion

We have developed a new spectroscopic technique for measuring the lateral sizes of hard X-ray sources that is based on the source broadening of spectral lines recorded behind the Rowland circle of modified Cauchois type spectrometers. The technique was enabled by a geometrical model of the line broadening mechanisms and was validated by comparisons with spectra from laboratory sources having known source sizes and direct measurements of detector resolution.

The lateral sizes of hard X-ray sources produced by the irradiation of solid targets by intense picosecond laser pulses were measured. The lateral extent of the hard X-ray emission, up to 0.5 mm from the focal spot, was measured from the source broadening of the spectral lines and from the relative emissions

from irradiated and spectator wires. The lateral emission sizes were consistent with energetic electron propagation through the target materials, with initial electron energies typically around 0.5 MeV.

The measurements of source size derived from the planar target spectra are based on the FWHM widths of the source-broadened spectral lines, and in this sense the measurements represent median values of the line widths, propagation range, and initial electron energy. The emission in the wings of the spectral lines indicate hard X-ray emission up to 1 mm lateral extent and generated by electrons up to 1 MeV energy. In addition, owing to the spectrometer viewing angle with respect to the target normal, the electron ranges and energies are likely much larger than those directly inferred from the observations. Similarly, the electron ranges derived from the wire targets have rather coarse spatial resolution resulting from the 0.5 and 0.125 mm wire diameters, and the electron range and energy may in fact be larger than the directly inferred values. Experiments with different laser beam, spectrometer, and target geometries are in progress and will provide more accurate measurements of the extent of the hard X-ray emission and the electron range and energy.

The weaker emission from targets containing good electrical insulators, compared to the emission from highly conducting target materials, implies inhibition of the electron propagation by the absence of a strong return current. This and other aspects of the K-shell emission, such as the dependence on the orientation of the wire targets relative to the electric field vector of the linearly polarized incident radiation, are the subjects of ongoing experiments. These experiments also include targets designed to study laser-induced energetic electron propagation through target materials, the dominant process in these high-field experiments, electron propagation along the target surface, and how to control these types of processes. Finally, other modeling approaches of the electron propagation, including Monte Carlo and particle in cell (PIC) codes, are necessary to have a better understanding of the lateral propagation of energetic electrons through the target materials and along the target surface.

Acknowledgements

We thank our colleagues who participated in all aspects of the work reviewed here: Csilla Szabo, Al Henins, Glenn Holland, Patrick Audebert, Erik Brambrink, Hye-Sook Park, Riccardo Tommasini, and many others. The work at NRL was supported by the Office of Naval Research. Certain commercial equipment, instruments, or materials are identified in this paper in order to specify the experimental procedure adequately. Such identification is not intended to imply recommendation or endorsement by the US government, nor is it intended to imply that the materials or equipment identified are necessarily the best available for the purpose.

References

- [1] Y. Cauchois, *J. de Physique*.3 (1932) 320 English translation is available at <http://spectroscopy.nrl.navy.mil/>.
- [2] A. Compton, S. Allison, in: *X-Rays in Theory and Experiments*, van Nostrand, New York, 1935 750.
- [3] L.T. Hudson, A. Henins, J.F. Seely, G.E. Holland, 15th International Conference on Atomic Processes in Plasmas, in: J.D. Gillaspay, J.J. Curry, W. Wiese (Eds.), *AIP Conference Proceedings* 926, American Institute of Physics, Melville, New York, 2007, pp. 34–41.
- [4] L.T. Hudson, A. Henins, R.D. Deslattes, J.F. Seely, G.E. Holland, R. Atkin, L. Martin, D.D. Meyerhofer, C. Stoeckl, *Rev. Sci. Instrum.* 73 (2002) 2270.
- [5] J.F. Seely, R. Doron, A. Bar-Shalom, L.T. Hudson, C. Stoeckl, *J. Quant. Spectr. Rad. Trans.* 81 (2003) 421.

- [6] J.F. Seely, C.A. Back, C. Constantin, R.W. Lee, H.-K. Chung, L.T. Hudson, C.I. Szabo, A. Henins, G.E. Holland, R. Atkin, L. Martin, *J. Quant. Spectr. Rad. Trans.* 99 (2006) 572.
- [7] L.T. Hudson, R. Atkin, C.A. Back, A. Henins, G.E. Holland, J.F. Seely, C. Szabo, *Rad. Phys. Chem.* 75 (2006) 1784.
- [8] C.I. Szabo, L.T. Hudson, A. Henins, G.E. Holland, R. Atkin, J.F. Seely, *Rad. Phys. Chem.* 75 (2006) 1824.
- [9] J.F. Seely, G. Holland, L. Hudson, C. Szabo, A. Henins, H.-S. Park, P. Patel, R. Tommasini, J. Laming, *High Energy Density Phys.* 3 (2007) 263.
- [10] R.D. Deslattes, J.C. Levin, M.D. Walker, A. Henins, *Med. Phys.* 21 (1994) 123.
- [11] C.T. Chantler, R.D. Deslattes, A. Henins, L.T. Hudson, *Br. J. Radiol.* 69 (1996) 636.
- [12] L.T. Hudson, R.D. Deslattes, A. Henins, C.T. Chantler, E.G. Kessler, J.E. Schweppe, *Med. Phys.* 23 (1996) 1659.
- [13] J.F. Seely, L.T. Hudson, G.E. Holland, A. Henins, *Appl. Opt.* 47 (2008) 2767.
- [14] J. Seely, G. Holland, L. Hudson, A. Henins, *Appl. Opt.* 47 (2008) 5753.
- [15] J.F. Seely, G. Holland, L. Hudson, C. Szabo, A. Henins, H.-S. Park, P. Patel, R. Tommasini, J. Laming, *High Energy Density Phys.* 3 (2007) 263.
- [16] J. Seely, C. Szabo, P. Audebert, E. Brambrink, E. Tabakhoff, G. Holland, L. Hudson, A. Henins, P. Indelicato, A. Gumberidze, *High Energy Density Phys.* 5 (2009) 263.
- [17] C. Szabo, et al., *Eur. Phys. J. ST* 169 (2009) 243.
- [18] J.D. Hares, J.D. Kilkenny, M.H. Key, J.G. Lunney, *Phys. Rev. Lett.* 42 (1979) 1216.
- [19] N.A. Ebrahim, C. Joshi, D.M. Villeneuve, N.H. Burnett, M.C. Richardson, *Phys. Rev. Lett.* 43 (1979) 1995.
- [20] Y. Sakagami, H. Kawakami, S. Nagao, *Phys. Rev. Lett.* 42 (1979) 839.
- [21] P. Kolodner, E. Yablonoich, *Phys. Rev. Lett.* 43 (1979) 1402.
- [22] A.W. Ehler, F. Begay, T.H. Tan, P.H. Castine, *J. Phys. D, Appl. Phys.* 13 (1980) L65.
- [23] R.F. Benjamin, G.H. McCall, A.W. Ehler, *Phys. Rev. Lett.* 42 (1979) 890.
- [24] P.A. Jaanimagi, N.A. Ebrahim, N.H. Burnett, C. Joshi, *Appl. Phys. Lett.* 38 (1981) 734.
- [25] K. Krushelnick, E.L. Clark, Z. Najmudin, M. Salvati, M. Santala, M. Tatarakis, A. Dangor, *Phys. Rev. Lett.* 83 (1999) 737.
- [26] F. Amiranoff, *Meas. Sci. Technol.* 12 (2001) 1795.
- [27] D. Batani, A. Antonicci, F. Pisani, A. Bernardinello, T. Hall, D. Scott, F. Amiranoff, M. Koenig, L. Gremillet, S. Baton, E. Martinolli, C. Rousseaux, and W. Nazarov, 5th Workshop on Fast Ignition of Fusion Targets (2001) 9–12.
- [28] H. Chen, S.C. Wilks, *Laser and Part. Beams* 23 (2005) 411.
- [29] W. Theobald, et al., *Phys. Plasmas* 13 (2006) 043102.
- [30] R. Tommasini, E. Fill, R. Bruch, G. Pretzler, *Appl. Phys. B* 79 (2004) 923.
- [31] H. Nishimura, et al., *Plasma Phys. Control Fusion* 47 (2005) B823.
- [32] Y.T. Li, et al., *Phys. Rev. Lett.* 96 (2006) 165003.
- [33] Z. Li, et al., *Phys. Plasmas* 13 (2006) 043104.
- [34] H. Habara, et al., *Phys. Rev. Lett.* 97 (2006) 095004.
- [35] L.M. Chen, et al., *Phys. Rev. Lett.* 100 (2008) 045004.
- [36] M.J. Berger, J.S. Coursey, M.A. Zucker, and J. Chang, "ESTAR, PSTAR, and ASTAR: computer programs for calculating stopping-power and range tables for electrons, protons, and helium ions (version 1.2.3)," 2005, available online at <http://physics.nist.gov/Star>. National Institute of Standards and Technology, Gaithersburg, MD. Originally published as M. J. Berger, NISTIR 4999, National Institute of Standards and Technology, Gaithersburg, MD (1993).